Research Article Vol. 60, No. 21 / 20 July 2021 / Applied Optics 6103

applied optics

Real-time holographic quantitative measurement of vapor density distribution of suspended droplets

Wei Song,[1,*] Qiusheng Liu,[2,3] Lixian Zhang,[1] Binbin Han,[1] and Lu Zhang[1]

[1]Technology and Engineering Center for Space Utilization, Chinese Academy of Sciences, Beijing 100194, China
[2]Institute of Mechanics, Chinese Academy of Sciences, Beijing 100190, China
[3]University of Chinese Academy of Sciences, Beijing 100049, China
*Corresponding author: songwei@csu.ac.cn

Received 13 May 2021; revised 11 June 2021; accepted 15 June 2021; posted 16 June 2021 (Doc. ID 431261); published 14 July 2021

We applied digital holography (DH) technology in a quantitative measurement of the density distribution of a low refractive index transparent substance (e.g., the vapor of suspended droplets). An optical setup was built based on the Mach–Zehnder interferometer. A measurement performance test showed the mean relative error of the measurement error was about 2.0%; that of the environment disturbance error was about 0.47%. By a quantitative method to assess the precision limit, the temperature measurement precision could achieve 0.01°C, and the vapor density measurement precision could achieve 0.0001 kg/m^3. We believe that all the benefits above make the setup a good choice for application in the Chinese space station.

https://doi.org/10.1364/AO.431261

1. INTRODUCTION

The Chinese space station (CSS), also known as the Tiangong space station, was launched in April 2021, providing an excellent research environment for microgravity science. Concerning investigations on liquid–gas systems, a two-phase system research rack (TPSR) has been planned and is being assembled. A crucial functional requirement of the TPSR is the measurement of the vapor density distribution of droplets.

The knowledge of density distribution for droplets vapor is crucial to study the transport of mass and heat in the gas–liquid phase; e.g., electronic chip cooling [1], digital microfluidic design [2], and the design of space environment control equipment [3]. Furthermore, the real-time quantitative measurement of vapor density could contribute to the precise control of droplet behaviors. In fact, the self-assembly of micro/nano materials can be realized by controlling the evaporation rate of droplets [4]. In addition, the logical editing of deoxyribonucleic acid (DNA) can be achieved by the generation, translocation, cleavage, and fusion of droplets carrying DNA molecules [5].

Real-time quantitative measurements of vapor density distribution also facilitate the development of the theoretical model for the gas–liquid phase, as well as the quantitative description of droplet evaporation and vapor condensation [6–8]. Some parameters that quantitatively describe the liquid in the gas–liquid phase process (i.e., the flow field), the temperature distribution, and the contact angle can be obtained by relatively simple detection schemes; e.g., particle image velocimetry (PIV) [9,10], infrared cameras or thermocouples [11], and microscopic optical systems [12]. In addition, even in a liquid–liquid system, droplets sizing and mixture fraction can be obtained by rainbow-angle diffractometry [13]. However, measurements on the gas side have rarely been considered to the best of our knowledge. On the one hand, they are more involved; on the other hand, the gas is overly sensitive to the influence of measurement tools. Actually, previous research focused on the contact angle, the surface tension, and other factors influencing the droplet behavior, but when a much more precise control is required, the influence of the vapor density distribution cannot be neglected.

As a noncontact and nondisruptive measurement method, optical interferometry is a very good choice to detect the properties of the gas phase [14]. According to the Gladstone–Dale law, there is a linear relation between the gas density and its refractive index [15,16], and thus quantitative density distribution can be obtained by optical measurements. In fact, the gas density distribution obtained by the optical interference method is an integral result of all the gas in the region that the objective beam goes through. However, the measurement results are still interesting because they represent the average value of the 2D distribution [17]. In addition, using this gas density distribution, the distribution of the temperature, pressure, and evaporation rate can be further worked out [18]. The experimental setup used in optical interferometry is usually the Mach–Zehnder interferometer [19,20], where the two interfering beams generate a group of vertical interference fringes that are exploited to obtain the diffusion coefficient via,

for instance, the FTP algorithm [21]. However, such fringes are easily affected by environmental noise, and every order Fourier spectrum of its Fourier transform is affected by the 0 order Fourier spectrum. By contrast, the interference fringes in DH usually have an inclination angle about 45°, and the fringe interval is two pixels [22]. In this way, the +1, 0, and −1 order Fourier spectrums in the Fourier transform of a hologram can be separated, where the +1 order Fourier spectrum can be extracted without crosstalk by a high-pass filter.

DH techniques have been applied to quantitative measurements of some physical parameters of high refractive index transparent substances; e.g., for measuring liquid concentration [23], multilayer temperature gradient in liquid [24], and density distribution of high-speed gas flow [25]. In particular, the gas density distribution of a jet flow in a supersonic airflow wind tunnel can be reliably reconstructed, and relevant details such as the boundary lines or shock and expansion waves are clearly observed [26]. In addition, a 3D reconstruction of axisymmetric gas density distribution can be obtained by a piece of 2D hologram [27]. The 3D distribution of a nonaxisymmetric, but stable, gas flow density can be acquired using hologram scanning together with the Tikhonov regularization algorithm [28]. For the gas density distribution of nonaxisymmetric and time-varying turbulent flow, 3D reconstruction can be obtained using a set of multi-angle holographic recording systems [29]. In fact, since DH records all-optical field information, the quantitative gas density distribution can be obtained whether the distribution is axisymmetric or nonaxisymmetric.

In this paper, we apply DH to the measurement of the vapor density distribution of a suspended droplet, and the droplet vapor is thought to be a medium with a weak refractive index dependency with temperature and density. We have built up an optical setup based on the Mach–Zehnder interferometer. The measurement performance of the setup has been assessed by comparing the measurement results of the temperature gradients distribution in deionized water with those obtained by thermocouples. It can be done because the liquid temperature also has a quantitative relation with the refractive index, though it is nonlinear [30,31]. This means that whether the measurement object is vapor density or liquid temperature, it is actually the refractive index measurement by the DH method. Subsequently, we determine the vapor density distribution of suspended FC72 droplets and discuss the experimental results. More specifically, FC72 is a clear, colorless, fully fluorinated liquid that is thermally and chemically stable, compatible with sensitive materials, nonflammable, nonconductive, practically nontoxic, and it leaves essentially no residue upon evaporation. The combination of these unique properties makes Fluorinert liquid FC72 ideal for research work on the liquid–gas phase [32,33], and can be safely applied in the manned spacecraft and manned laboratory [34,35].

Table 1. Parameters of Setup in Fig. 1

Item	Focal Length (mm)	Aperture (mm)	Position (mm)
L2	200	50.8	0
L3	−250	50.8	50
L4	150	50.8	65
L5	150	50.8	0
L6	100	50.8	250

2. EXPERIMENTAL SETUP AND PROCEDURES

A. Experimental Optical Setup

The scheme of our optical setup for off-axis DH based on the Mach–Zehnder interferometer is shown in Fig. 1(a). A laser beam is split into an objective beam and a reference beam by a polarized beam splitter (PBS) after expansion and collimation via a beam expander (BE), aperture (AP), and lens L1. The intensity ratio of the two beams can be adjusted by a half-wave plate (HWP1). The objective beam passes through the experimental sample, and its phase is modulated by the refractive index distribution of the sample. Then, the sample is imaged on the camera by the lenses combination of L2, L3, and L4 [36], which is convenient to adjust the magnification. The diameter of the reference beam is adjusted by the lens combination of L5 and L6 to match the objective beam size on the camera. The polarization of the reference beam is adjusted by HWP2 to be consistent with that of the objective beam. Finally, by adjusting the deflection angles of mirror M2 and the nonpolarized beam splitter (NPBS), the reference beam propagation path is changed and the reference beam overlaps the objective beam on the camera. Thus, a hologram is recorded. More specifically, the main parameters (focal lengths, positions, and apertures of L2, L3, . . . , L6) of the setup are shown in Table 1. The "Position" in Table 1 denotes the distance between the two adjacent lenses; e.g., L6's "Position" is 250 mm, meaning that the distance between L5 and L6 is 250 mm. In particular, the "Position" is 0 for L2 and L5 because the beams reaching them are collimated, which means L2, L5, and the subsequent parts can move freely along the laser beam to accommodate the size of the experimental device that contains a sample.

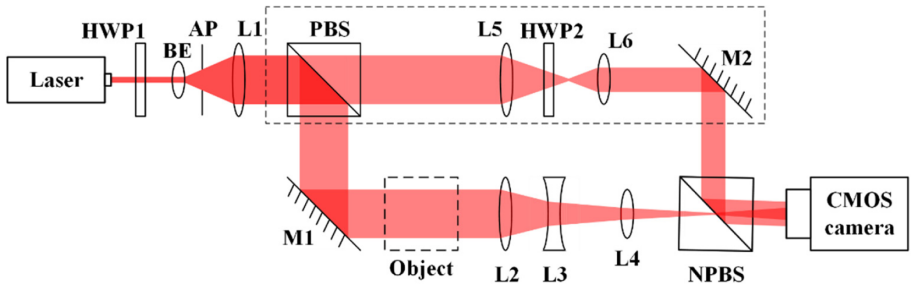

Fig. 1. (a) Schematic diagram of the optical setup. HWP, half-wave plate; BE, beam expander; AP, aperture; L, lenses; PBS, polarized beam splitter; NPBS, non-polarized beam splitter; and M, mirror.

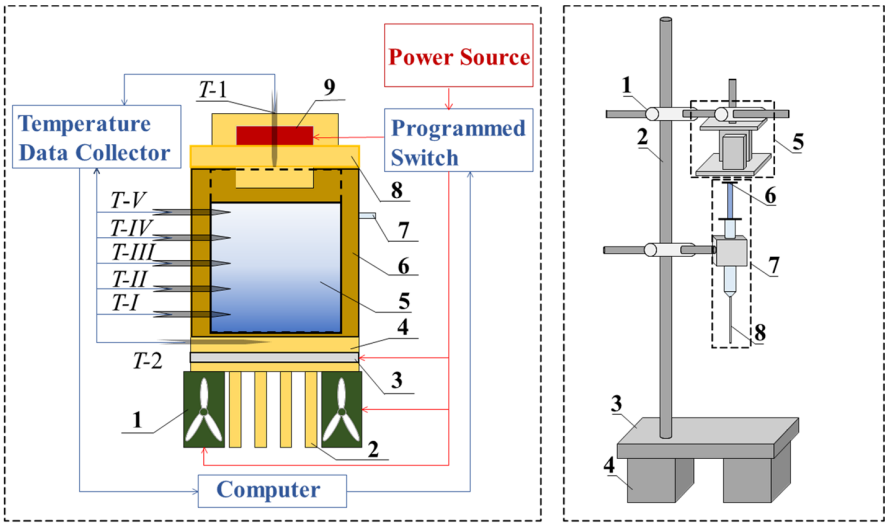

(a) (b)

Fig. 2. Schematic diagram of the experimental devices. (a) Device used as an assessment tool for the optical setup. 1: cooling fans; 2: copper fins; 3: thermo-electric cooler (TEC); 4: copper bottom; 5: quartz glass window; 6: side-wall of the thermal insulation material; 7: input port; 8: copper cover; 9: heating plate, T1 and T2; and $T-I \sim T-V$: thermocouples. (b) Device used for the droplet vapor density measurement. 1: fixed 90° bracket; 2: post; 3: universal base plate (UBP); 4: heavy-duty switchable magnetic base (MB); 5: micrometer positioning stage (MPS); 6: plunger rod (PR); 7: injector; and 8: needle.

In general, the hologram must subtract the background information that was introduced by the optical setup. The background information subtraction can be done by a two-step method [37]. A hologram before the experiment is first recorded to reconstruct the background information. Second, the background information is removed from the holograms subsequently recorded during the experiment.

B. Experimental Devices

We specifically design a water chamber to assess the performance of the optical setup, as shown in Fig. 2(a). The water chamber is filled with deionized water from the input port (No. 7). The excess liquid and the displaced air are discharged from the output port (No. 8). Then we put a copper cover (No. 9) on top of the chamber, which includes a piece of heating plate (No. 10). A piece of thermo-electric cooler (TEC) (No. 3) with cooling fans (No. 1) and copper fins (No. 2) is installed on the bottom of the chamber (No. 4). The thermocouples on one side of the chamber (No. $T-I \sim V$) are arranged at different depths in the water to record the time-dependent temperature distribution. The other thermocouples (No. $T-1$ and $T-2$) are used to provide the temperatures of the copper cover (No. 9) and the bottom of the chamber (No. 4) to the feedback control system [the blue parts in Fig. 2(a)], so that the temperatures in the top and bottom remain stable. Additionally, the chamber has two optical quartz windows (No. 5), so that the objective beam can go through the water to acquire information about the temperature gradient field.

To realize real-time measurement of the vapor density distribution of suspended FC72 droplets, a droplet generator is assembled, as shown in Fig. 2(b). The generator is assembled using several components. The most important one is a syringe (No. 7) that stores the FC72 liquid. When the FC72 liquid is exhausted, the syringe can be replenished. A droplet can be produced by pushing the plunger rod (PR) (No. 6) forward about 1.5 mm. To balance the capillarity and prevent resorption of the droplets, the PR position is maintained by a high-torque micrometer positioning stage (MPS) (No. 5). Moreover, the whole generator is installed on a universal base plate (UBP) (No. 3) with two heavy-duty magnetic bases (MB) (No. 4) to isolate high-frequency vibrations from the environment and avoid the suspended droplet falling due to disturbance.

C. Experimental Procedures

1. Measurement Performance Assessment

The temperature gradient field distribution in the water chamber can be recorded by DH and thermocouples simultaneously for comparison. However, the water flows easily and it often contains air, which comes out and makes bubbles, having an influence on the measurement.

To remove bubbles, we preheated the deionized water to about 40°C and waited for a natural cooling to the environment temperature about 25.2°C. This preheating and cooling process has been repeated two times to make sure that no obvious bubbles came out.

To keep the water stable, the water chamber has been designed with heating on the top and cooling on the bottom. In this way, the denser cold water tends to stay at the bottom, and the less dense density warm water tends to float on the top. The temperature is almost constant at a fixed depth, which means that the water is in a quasi-stationary state. A stable temperature gradient field without buoyancy convection, but with multiple different temperature layers could be produced [38]. Additionally, when the heating and cooling stop, there is only slow diffusion because of the temperature difference, rather than

obvious flows. The temperature gradient field would gradually dissipate to be uniform.

What is more, we performed the experiment at midnight to minimize the impact of environmental vibration. The chamber was also installed on a heavy UBP with two MBs to isolate it from the environment.

With the consideration above, we took a background hologram (H_0) when the water's temperature was uniform at the temperature T_0, which can be confirmed by a thermocouples $T-I\sim V$ reading out the same temperature $T_0=25.2°\mathrm{C}$. Then we heated the copper cover (No. 8) to 40°C and cooled the copper bottom (No. 4) to 15°C to obtain a stable temperature gradient field. During the formation of the temperature gradient field, only thermocouples record temperature data every second. But in the subsequent temperature gradient field dissipation, the holograms were also recorded every second. Specifically, the background hologram H_0 contained the phase distribution of the experiment sample that was the deionized water with a uniform temperature. What is more, H_0 also contained various phase distortions and spherical aberrations, noises from the environment, and other phase information unrelated to the experiment.

2. Measurement of the Suspended Droplet Vapor Density Distribution

Different from the measurement performance test, when there were no droplets or vapor, we started to record holograms, and then pushed the rod forward about 1.5 mm to produce suspended droplets. Holograms were recorded every 0.2 s until the droplets evaporated and disappeared. Before the vapor density measurement started, we waited for the environment to stabilize, which can be confirmed by the temperature T, pressure p, and humidity rh reading staying constant in the lab. The first recorded hologram was the background hologram (H_0). Specifically, in this experiment, H_0 contained the phase distribution of the environment air, in addition to distortions, spherical aberrations, noises, and other unrelated phase information. However, H_0 did not contain the experiment sample that was a FC72 droplet or vapor.

3. DATA PROCESSING METHODS

The hologram $H(x,\ y)$ recorded by the camera can be expressed as [39]

$$H(x,y)=|O(x,y)+R(x,y)|^2=|O(x,y)|^2+|R(x,y)|^2+O(x,y)\cdot R^*(x,y)+O^*(x,y)\cdot R(x,y), \tag{1}$$

where $O(x,\ y)$ and $R(x,\ y)$ denote the complex amplitude distribution of the objective and reference beam, respectively. The symbol * denotes complex conjugation. In the Fourier spectrum of $H(x,\ y)$, there are -1, 0, and $+1$ order spectrums separated each other [22,40]. The 0 order spectrum $F[|O(x,\ y)|^2+|R(x,\ y)|^2]$ corresponds to the energy of the two beams, and contains no phase information. The -1 order spectrum $F[O^*(x,\ y)\cdot R(x,\ y)]$ is the conjugate of the $+1$ order spectrum $F[O(x,\ y)\cdot R^*(x,\ y)]$. Both -1 and $+1$ order spectrums contain the phase information, but generally, the information $I(x,\ y)$ (also referred to as the reconstructed information), is reconstructed by the inverse Fourier transform of the $+1$ order spectrum [40,41]:

$$F[H(x,y)]=F[|O(x,y)|^2+|R(x,y)|^2]+F[O(x,y)\cdot R^*(x,y)]+F[O^*(x,y)\cdot R(x,y)]$$
$$I(x,y)=F^{-1}\left\{F[O(x,y)\cdot R^*(x,y)]\right\}. \tag{2}$$

The background information I_0 is correspondingly obtained from the background hologram H_0. As mentioned above, the information obtained from the other recorded holograms is divided by I_0 to subtract the background. The phase information $\Delta\varphi_{\mathrm{obj}}(x,\ y)$ is thus obtained as [42,43]

$$\Delta\varphi_{\mathrm{obj}}(x,y)=\arctan\left\{\frac{\mathrm{Im}\,[I(x,y)/I_0(x,y)]}{\mathrm{Re}\,[I(x,y)/I_0(x,y)]}\right\}+\Delta\varphi_{2\pi}(x,y), \tag{3}$$

where $\Delta\varphi_{2\pi}(x,\ y)$ denotes the phase compensation term determined by the arc tangent results. The refractive index distribution $n_{\mathrm{obj}}(x,\ y)$ is then given by [39]

$$\bar{n}(x,y)=\frac{\lambda\Delta\varphi_{\mathrm{obj}}(x,y)}{2\pi d_0}+n_0, \tag{4}$$

where d_0 is the distance that the objective beam propagates in the transparent substance, n_0 denotes the uniformly distributed refractive index in the background hologram. Finally, the temperature distribution $T(x,\ y)$ or the gas density distribution $\rho(x,\ y)$ can obtained from their relations with the refractive index $n(x,\ y)$ (see Section 5 for details).

4. EXPERIMENTAL RESULTS AND DATA ANALYSIS

A. Measurement Performance Test

1. Test Results

In the measurement performance test, holograms were only recorded when the temperature gradient field was dissipating. One hologram was recorded every second, and a total of 3,400 holograms were recorded. The data processing for each hologram is shown in Figs. 3(a)–3(e). The positions of the thermocouples are labeled in the original hologram, shown in Fig. 3(a), to facilitate the following comparison of the temperature data. Upon zooming in Fig. 3(a), it could be observed that interference fringes have an inclination angle about 45° and the fringes interval is about 2 pixels, so that the $+1$ order Fourier spectrum can be extracted via high-pass filtering and is weakly affected by the 0 order Fourier spectrum, as shown in Fig. 3(b). The Fourier transform of the hologram is obtained by fast Fourier transform (FFT), as also shown in Fig. 3(b), where the $+1$, 0 and -1-order Fourier spectrums are separated from each other. Figure 3(c) shows the distribution of the complex amplitude, which is obtained by the inverse FFT (IFFT) operation of the second extracted $+1$ order Fourier spectrum. Figure 3(d) exhibits the distribution of the wrapped phase obtained by the arc tangent operation of the complex

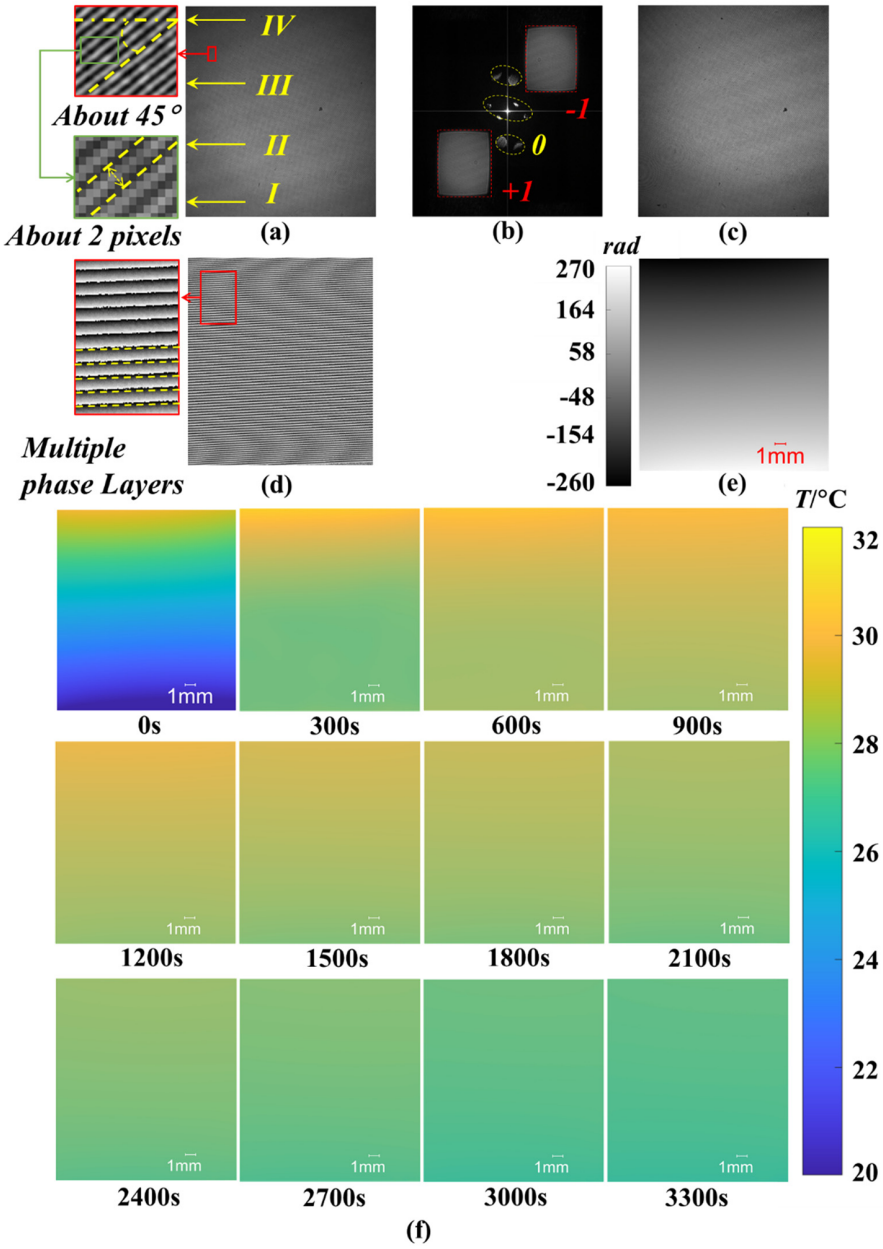

Fig. 3. Graphical representations of the data processing steps. (a) Hologram recorded at 0 s, (b) Fourier spectra of (a), (c) complex amplitude reconstructions of (a), (d) wrapped phase of (c), (e) unwrapped phase of (d), and (f) temperature distributions every 300 s during 3–3300 s.

data in Fig. 3(c). Multiple phase layers can be clearly observed in the grayscale of the wrapped phase, which implies that there are different temperature layers and the temperature in each layer is almost identical. The distribution of the unwrapped phase obtained by the phase unwrapping algorithm LS-DCT [44] is shown in Fig. 3(e). The unwrapped phase is smoothly distributed without any apparent singular point, which suggests that the phase unwrapping algorithm is reliable. Finally, the refractive index distribution $n(x, y)$ is worked out according to Eq. (4). By the nonlinear quantitative relation between the refractive index and temperature (Section 5.A), the temperature distribution [Fig. 3(f)] is obtained. In agreement with our theoretical anticipation, no obvious buoyancy convection can be seen during the dissipation of the temperature gradients, and the temperature distribution gradually becomes uniform.

2. Preliminary Analysis

As shown in Fig. 4(a), the temperature gradient gradually vanishes after the heating/cooling system is switched off. In particular, after 3400 s, the temperature distribution is almost uniform and the temperature difference between the top and the bottom of the chamber is less than 0.8°C. However, a temperature gradient field still can be identified, shown by the blue points in Fig. 4(b). The data is from the orange line in Fig. 4(a). Upon inspecting the blue points in Figs. 4(b)–4(d), it seems that, as the accuracy of temperature data increases, the

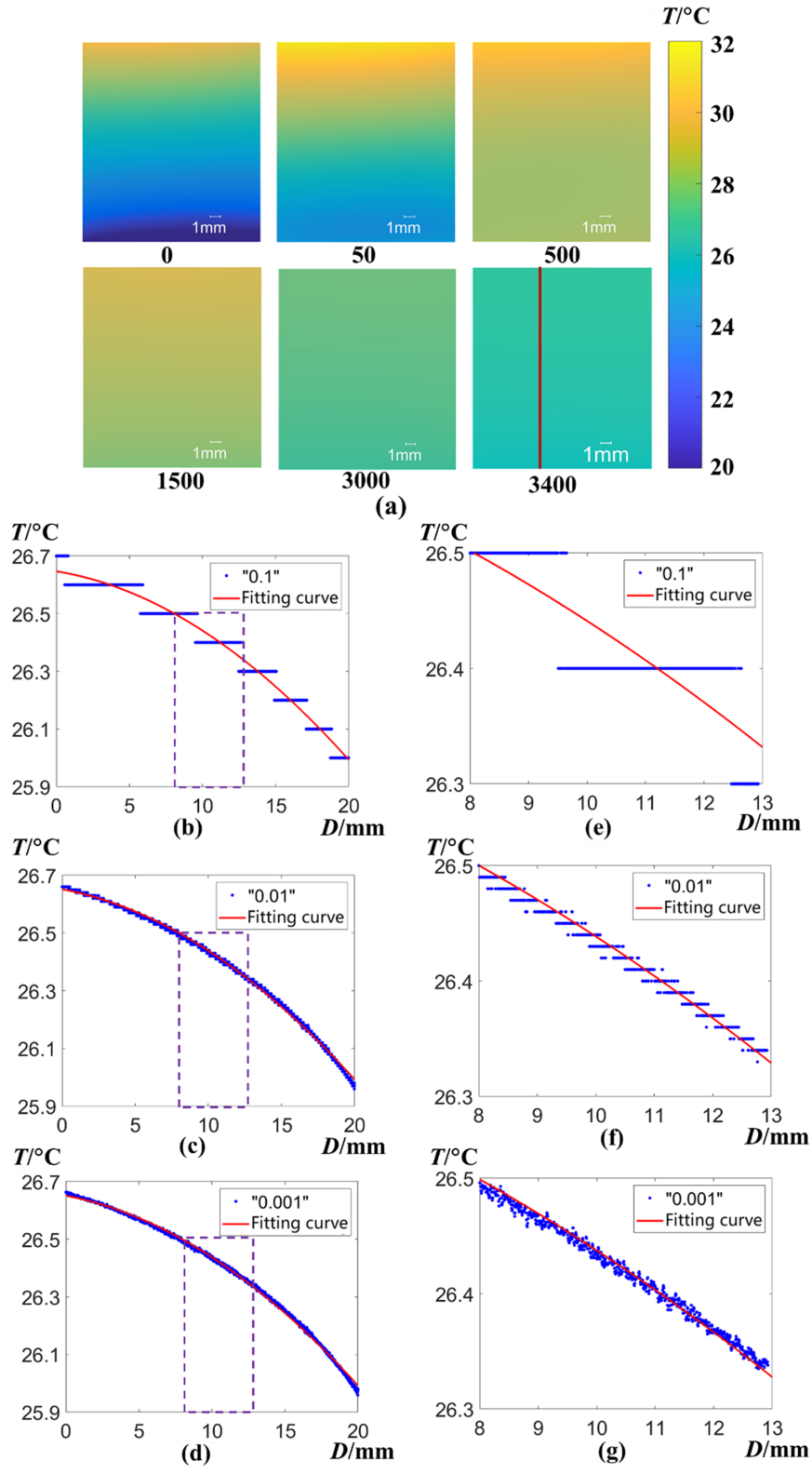

Fig. 4. Temperature distributions. (a) Temperature distributions at unequal time interval, (b) temperature gradient at time 3400 s [data of the orange line of (a)] with 10^{-1} accuracy, (c) same data with 10^{-2} accuracy, (d) same data with 10^{-3} accuracy, and (e)–(g) partial enlargement of the curves in (b)–(d), respectively.

temperature layers increase. But, if we enlarge these pictures [see the blue points in Figs. 4(e)–4(g)], it can be observed that the temperature layers first increase, but then become difficult to identify. Such a phenomenon implies that the measurement precision has a limit, which can be obtained by a quantitative analysis as follows.

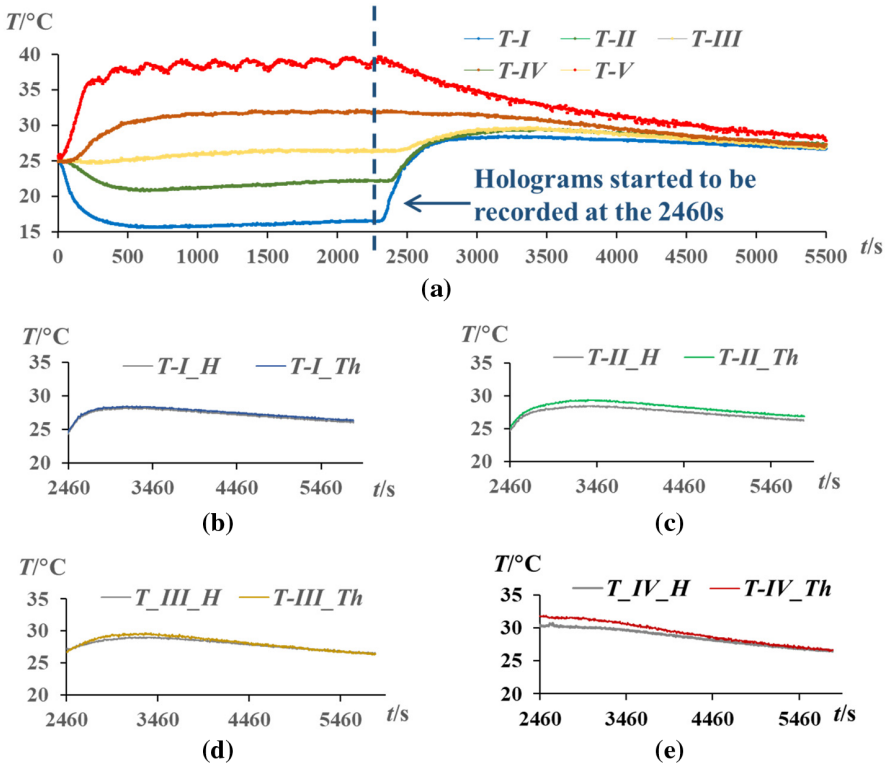

Fig. 5. Temperature data recorded by the thermocouples and obtained by DH method. (a) Data recorded by the thermocouples during the temperature gradient field formation and dissipation. (b)–(e) Comparison of the temperature data of thermocouples *T-I*, *T-II*, *T-III*, and *T-IV*, respectively.

Table 2. RMSE and Fitting Parameters a, b, and c of the Fitting Curves in Fig. 5 with Different Precisions

Item	"0.1"	"0.01"	"0.001"
a	26.66	26.67	26.67
b	−3.282	−3.925	−3.989
c	146.3	149.2	149.5
RMSE	0.03	0.008	0.007

The precision limit analysis model is expressed as

$$T = a \exp\left[-\left(\frac{D-b}{c}\right)^2\right], \tag{5}$$

where T represents temperature, D refers to the depth of water, and a, b, c are constants. The fitting curves for the temperature data with precisions from 10^{-1} to 10^{-3} are shown in Figs. 4(b)–4(d) (red lines). As shown in Table 2, the RMS error (RMSE) of the fitting curves [Figs. 4(b)–4(d)] quickly reduces and then saturates, which clearly suggests that the precision limit in the temperature distribution measurement is on the order of 0.01°C.

The comparison between the temperature data recorded by the thermocouples and that obtained by DH is shown in Fig. 5. More specifically, Fig. 5(a) shows the temperature data recorded by the thermocouples during the temperature gradient formation and dissipation. The first hologram was recorded when the temperature gradient began to dissipate at 2460 s. Only the temperature data of thermocouples $T-I-IV$ are compared due to the view field limit in holograms, as shown in Figs. 5(b)–5(e). The mean relative errors (MREs) are shown in Table 3. The maximum is about 2.56%, and the global average is about 2%.

Table 3. MRE of Measurement Error Through the Comparison of Temperature Data Obtained by Thermocouples and DH Method

Item	T-I	T-II	T-III	T-IV	Total
MRE	1.12%	2.69%	1.28%	2.56%	2.00%

B. Measurement of Gas Density Distribution

1. Experimental Results

The real-time vapor density distribution of the suspended FC72 droplet is shown in Fig. 6. Five holograms are recorded every second, and a total of 330 holograms are recorded. The processing of each hologram shown in Figs. 6(a)–6(e) is similar to that described above in Figs. 3(a)–3(e). More specifically, due to the application of the same optical setup, upon zooming in Fig. 6(a), the interference fringes in the original hologram have the same inclination angle (about 45°) and the fringes interval is about two pixels. Figure 6(b) shows the Fourier transform of Fig. 6(a), where the positions of +1, 0, and −1 order Fourier spectrums are basically the same as those in Fig. 4(b). The complex amplitude distribution [Fig. 6(c)], the distributions of the wrapped phase [Fig. 6(d)], and the unwrapped phase [Fig. 6(e)] are all obtained by the same operations and algorithms used in

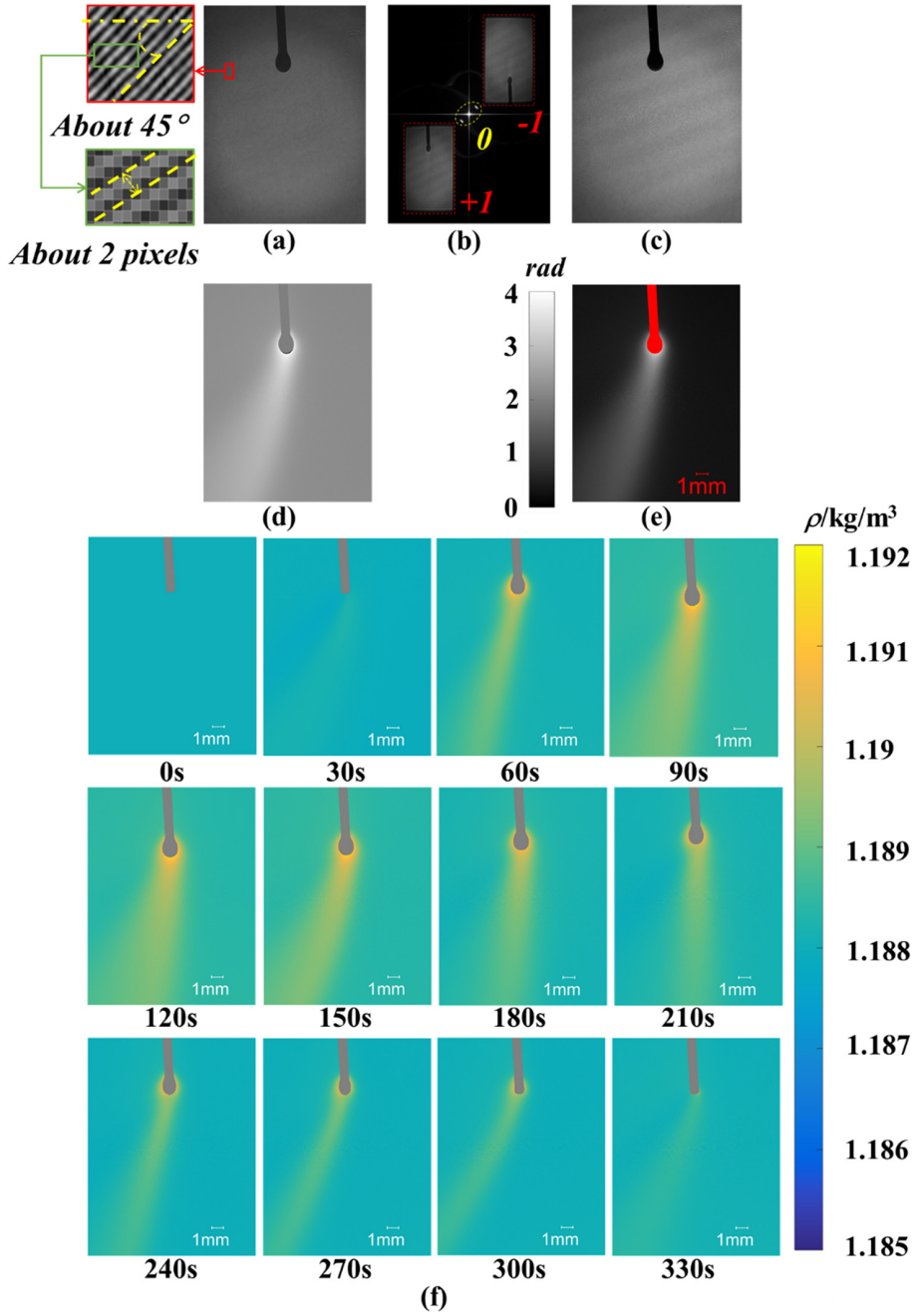

Fig. 6. Data processing for the gas density measurement. (a) Hologram recorded at 100 s, (b) Fourier spectra of (a), (c) complex amplitude reconstructions of (a), (d) wrapped phase of (c), (e) unwrapped phase of (d), and (f) gas density distribution every 30 s from time 0 to 330 s.

the measurement performance test above. Unlike the wrapped phase in Fig. 3(d), the wrapped phase in Fig. 6(d) has only one bright area and one dark area that can be distinguished, indicating that the phase change is less than 2π, which meets the anticipation of a low refractive index for the droplet vapor. In addition, the distribution of the unwrapped phase [Fig. 6(e)] is similar to that of the wrapped phase [Fig. 6(c)], which again confirms that the phase distribution variation is less than one 2π period, and the droplet vapor is characterized by a low refractive index. The refractive index distribution $n(x, y)$ could be worked out according to Eq. (4). By the linear quantitative relation between the refractive index and the gas density (Section 5.B), the vapor density distribution [Fig. 6(f)] also can be obtained.

2. Preliminary Analysis

Figure 7(a) shows a complete vapor density measurement procedure. The vapor gradually came out as we injected FC72 liquid to generate a droplet. After the injection stopped, the droplet shrank quickly as the vapor dissipates rapidly. Following the method above for quantitative analysis of the accuracy limit, the precision limit analysis model for vapor density measurement could be expressed as

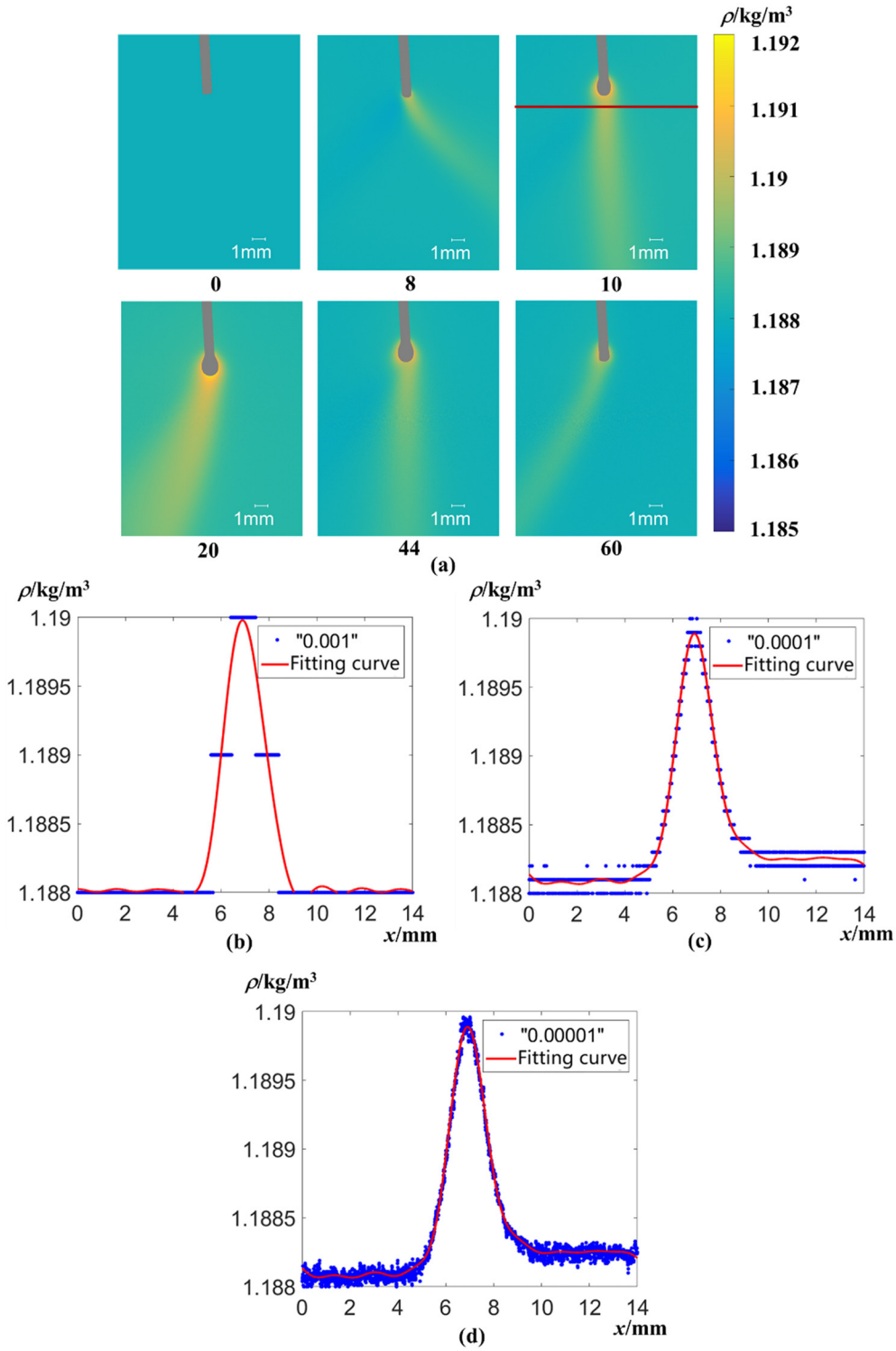

Fig. 7. Droplet vapor density distribution. (a) Vapor density distributions with an unequal time interval, (b) vapor density distribution with 10^{-3} accuracy, (c) same data with 10^{-4} accuracy, and (d) same data with 10^{-5} accuracy.

$$\rho = \rho_0 + \sum_{i=1}^{8} [a_i \cos(iwx) + b_i \sin(iwx)], \quad (6)$$

where ρ represents the gas density, ρ_0, a_i, and b_i are constants, and i ranges from 1 to 8. The fitting curves for the vapor density with precisions from 10^{-3} to 10^{-5} are shown in Figs. 7(b)–7(d) (red lines). According to the RMSE in Table 4 of the fitting curves in Figs. 7(b)–7(d), the precision limit in the vapor density measurement is on the order of 0.0001 kg/m^3.

Table 4. RMSE and Fitting Parameters ρ_0, a_i, b_i, and w of the Fitting Curves in Fig. 8 with Different Precisions

Item/kg/m^3	"10^{-3}"	"10^{-4}"	"10^{-5}"
a_0	1.19E + 00	1.19E + 00	1.19E + 00
a_1	−5.37E − 04	−4.42E − 04	−4.43E − 04
b_1	−5.72E − 05	−4.80E − 05	−4.85E − 05
a_2	4.44E − 04	3.47E − 04	3.47E − 04
b_2	9.47E − 05	−9.72E − 05	−9.95E − 05
a_3	−3.19E − 04	−2.55E − 04	−2.54E − 04
b_3	−1.01E − 04	7.39E − 05	7.51E − 05
a_4	1.93E − 04	1.54E − 04	1.52E − 04
b_4	7.79E − 05	−1.02E − 04	−1.04E − 04
a_5	−9.35E − 05	−9.04E − 05	−8.93E − 05
b_5	−3.90E − 05	6.87E − 05	6.96E − 05
a_6	3.33E − 05	4.46E − 05	4.26E − 05
b_6	2.68E − 06	−5.84E − 05	−5.91E − 05
a_7	−1.31E − 05	−2.49E − 05	−2.58E − 05
b_7	1.46E − 05	3.19E − 05	3.20E − 05
a_8	1.72E − 05	5.37E − 06	5.59E − 06
b_8	−7.79E − 06	−2.43E − 05	−2.36E − 05
w	4.66E − 01	4.36E − 01	4.36E − 01
RMSE	1.53E − 04	5.01E − 05	3.95E − 05

5. DISCUSSION

As mentioned above, the liquid temperature has a nonlinear quantitative relationship to its refractive index, whereas the gas density has a linear quantitative relationship to its refractive index. In the following, we individually discuss specific numerical calculation methods for the two relationships. We also discuss the effect of the environment disturbance.

A. Nonlinear Quantitative Relationship between Temperature and Refractive Index of Deionized Water

Although the Lorentz–Lorenz formula [30] says that the refractive index n depends nonlinearly on the temperature T, the quantitative relation could be obtained by a polynomial fitting method [31,45] with all the data listed in Table 5. These data come from the "CRC Handbook of Chemistry and Physics" [46]. These data were obtained by formulations [47], and

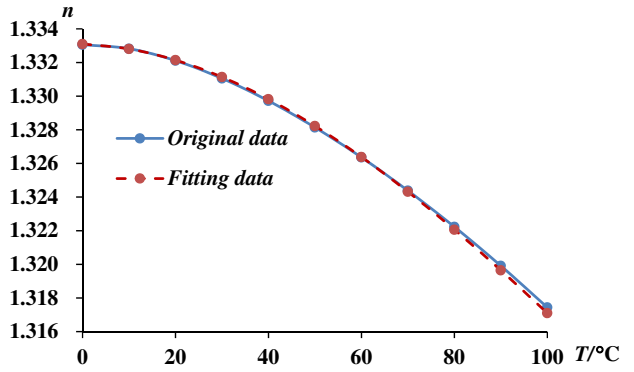

Fig. 8. Quantitative relationship between refractivity and water temperature.

between 5°C and 60°C in the visible wavelength was much more reliable with an uncertainty of 6×10^{-6}.

In our experiments the optical wavelength is 632.8 nm, and the range of temperatures is 15°C–40°C; and both of them are well within the high reliable data range in Table 5. A cubic polynomial fitting result is obtained with the data at wavelength 632.8 nm in Table 5 and is given by

$$n(T) = a_1 T^3 + a_2 T^2 + a_3 T + n_c, \tag{7}$$

where $a_1 = 5 \times 10^{-9}$, $a_2 = -2 \times 10^{-6}$, $a_3 = -1 \times 10^{-5}$, and $n_c = 1.3331$. n_c is refractive index of the fitting curve when T is 0 and the wavelength is 632.8 nm. Although it is not the exact value 1.33306 in Table 5, the conformity 1-(|1.3331-1.33306|/1.33306) is higher than 99.99%. Figure 8 shows the curves of the fitting data and original data.

The correlation coefficient r of the fitting curve is

$$r_{n,n_{\text{Table}}} = \frac{\sum_{i=1}^{N} (n_i - \bar{n})(n_{\text{Table}i} - \bar{n}_{\text{Table}})}{\sqrt{\sum_{i=1}^{N} (n_i - \bar{n})^2}\sqrt{\sum_{i=1}^{N} (n_{\text{Table}i} - \bar{n}_{\text{Table}})^2}} \times 100\%, \tag{8}$$

where n is the refractivity data of the fitting curve, and n_{Table} is the data in 632.8 nm in Table 5. $N = 11$ is the total amount of data in one column of Table 4. It is obtained that $r \cong 99.99\%$, which indicates that Eq. (7) has well described the nonlinear quantitative relation between the temperature and refractive index in deionized water. Combining Eq. (4) with Eq. (7), the temperature can be expressed as

Table 5. Water Refractive Index Dependency with Temperature and Wavelength[a]

T/°C	226.50 nm	361.05 nm	404.41 nm	589.00 nm	632.80 nm	1.01398 mm
0	1.3945	1.34896	1.34415	1.33432	1.33306	1.32612
10	1.39422	1.3487	1.34389	1.33408	1.33282	1.32591
20	1.39336	1.34795	1.34315	1.33336	1.33211	1.32524
30	1.39208	1.34682	1.34205	1.3323	1.33105	1.32424
40	1.39046	1.3454	1.34065	1.33095	1.32972	1.32296
50	1.38854	1.34373	1.33901	1.32937	1.32814	1.32145
60	1.38636	1.34184	1.33714	1.32757	1.32636	1.31974
70	1.38395	1.33974	1.33508	1.32559	1.32438	1.31784
80	1.38132	1.33746	1.33284	1.32342	1.32223	1.31576
90	1.37849	1.33501	1.33042	1.32109	1.31991	1.31353
100	1.37547	1.33239	1.32784	1.31861	1.31744	1.31114

[a]From [46]

$$T = Y - \frac{a_2}{3a_1},\ Y = 2\sqrt{-p}\cos(\alpha + 240°),\ \alpha = \frac{1}{3}\arccos\frac{-q\sqrt{-p}}{p^2}, \tag{9}$$

where p and q are expressed as

$$p = \frac{a_3}{3a_1} - \frac{a_2^2}{9a_1^2},\ q = \frac{n_0 - \bar{n}}{2a_1} + \frac{a_2^3}{27a_1^3} - \frac{a_2 a_3}{6a_1^2}. \tag{10}$$

When the deionized water temperature is uniform at $T_0 = 25.2°C$, the n_0 in Eq. (4) can be defined by Eqs. (9) and (10). d_0 is defined as the width of the chamber [see Fig. 2(a)] and $d_0 = 30$ mm.

B. Linear Quantitative Relationship between Gas Density and Refractive Index

According to the Gladstone–Dale law [48], the linear relationship between gas density ρ and refractive index n is expressed by

$$n(\rho) = 1 + K_{GD}\rho, \tag{11}$$

where K_{GD} stands for the Gladstone–Dale constant, depending on the measurement wavelength λ, as [49]

$$K_{GD}(\lambda) \cong 2.24 \times 10^{-4} \cdot \left(1 + \frac{7.52 \cdot 10^{-3}}{\lambda^2}\right) (m^3/kg), \tag{12}$$

where the λ unit is μm. In this paper, the measurement wavelength λ is 632.8 nm, so the K_{GD} is about 2.28×10^{-4} m^3/kg. For convenience, combined with Eq. (4), Eq. (11) also could be expressed as

$$\rho\ (n) = \frac{\bar{n} - 1}{K_{GD}}. \tag{13}$$

Before the droplet generates and the vapor comes out, the uniform air density ρ_0 can be worked out according to CIPM-81/91 [50–53] as

$$\rho = \frac{0.34848p - 0.009\ (rh) \times \exp(0.062T)}{273.15 + T}, \tag{14}$$

where p denotes the ambient pressure (mbar), rh is the relative humidity (%), and T is environmental temperature (°C). Using the laboratory environment parameters $p \cong 1013$ atm, $rh \cong 40\%$ and $T \cong 25°C$, we obtain $\rho_0 \cong 1.184\ kg/m^3$. Substituting the ρ_0 into Eq. (11), n_0 could be obtained. d_0 is defined as the distance between mirror M1 and lens L2 in Fig. 1(a) and $d_0 = 400$ mm.

C. Effect of Environment Disturbance

In the vapor density distribution measurement, the background hologram (H_0) contained no sample (a droplet and its vapor). However, in the performance test, the background hologram (H_0) contained a sample (the 25.2°C deionized water) that indicated the water temperature measurement was actually a relative measurement. Such a relative measurement offers a chance to assess the influence of environment disturbances on our optical setup. Therefore, with a new data processing method, we reprocessed the holograms recording the deionized water temperature changes. The new data processing method only changes the way to obtain the phase as follows. The kth hologram phase distribution $\Delta\varphi_{obj k}(x, y)$ is obtained by summing $\Delta\varphi_{obj k-1}(x, y)$ and $\Delta\varphi_k(x, y)$ and is expressed as

$$\Delta\varphi_k(x, y) = \arctan\left\{\frac{\mathrm{Im}\left[I_k(x, y)/I_{k-1}(x, y)\right]}{\mathrm{Re}\left[I_k(x, y)/I_{k-1}(x, y)\right]}\right\} + \Delta\varphi_{2\pi}(x, y),\ k = 1, 2, \ldots, N$$

$$\Delta\varphi_{obj_k}(x, y) = \Delta\varphi_{obj_{k-1}}(x, y) + \Delta\varphi_k(x, y), \tag{15}$$

where N is the total number of the recorded holograms, except the background hologram H_0. $\Delta\varphi_{obj k-1}(x, y)$ is the phase distribution of k-1th hologram. $\Delta\varphi_k(x, y)$ is the phase difference between the kth and the k-1th hologram. Therefore, the new

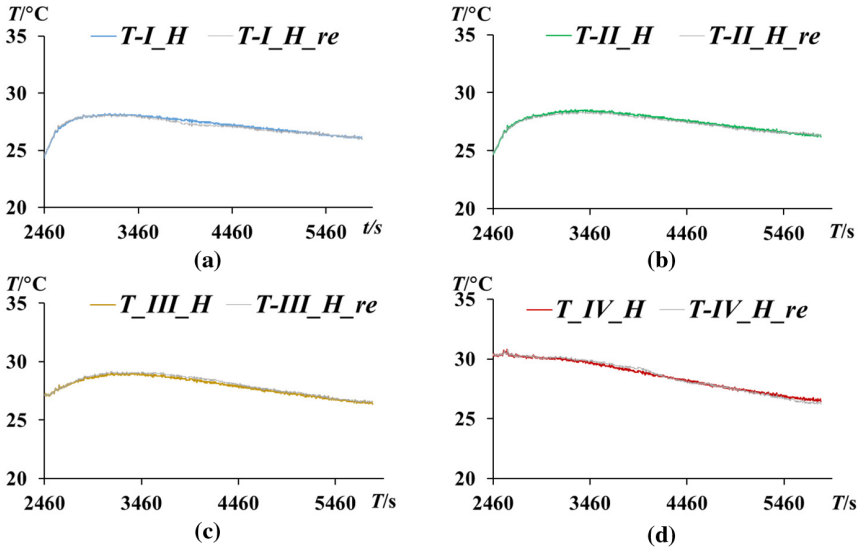

Fig. 9. Comparison of the temperature data by the old data processing method and the new one. (a)–(b) Comparison of data at the thermocouple positions *T-I*, *T-II*, *T-III*, and *T-IV*, respectively.

Table 6. MRE of the Environment Disturbance Error through the Comparison of the Temperature Data Obtained by the Two Different Data Processing Methods

Item	T-I	T-II	T-III	T-IV	Total
MRE	0.45%	0.43%	0.47%	0.52%	0.47%

data processing method only requires replacing Eq. (3) with Eq. (15), and the other steps remain the same.

The comparison between the temperature data obtained using the old data processing method and that obtained with the new one is illustrated in Fig. 9, where $T - I_H \sim T - IV_H$ are the data using the old method, and $T - I_{Hr}e \sim T - IV_{Hr}e$ are the results using the new one. The MREs are shown in Table 6. The maximum is about 0.52% and the global average is about 0.47%, which means that the environment influence on our setup is limited, and the temperature results in the measurement performance test are reliable.

6. CONCLUSION

In this paper, we have built an optical setup based on the Mach–Zehnder interferometer. The measurement performance of the setup has been assessed by comparing the measurement results of the distribution of temperature gradients by thermocouples and by the DH method. The comparison has shown that the MRE of the measurement error was about 2.0%, and the MRE of the environment disturbance error was about 0.47%. This indicates that our setup could be reliably used in the real-time measurement of vapor density distribution of suspended droplets.

A quantitative method to assess the precision limit has been applied, in which the accuracy corresponds to the saturation point of the RMSE of the fitting parameters. The measurement precision of our optical setup is on the order of 0.01°C for temperature distribution and about 0.0001 kg/m^3 for gas density distribution. In addition, the vapor density measurement results have shown that the phase distribution was less than one 2π period; i.e., the droplet vapor has a low refractive index.

In conclusion, we have successfully applied the DH technique to quantitatively measure the density distribution of a low refractive index transparent substance (i.e., the droplet vapor) and we have performed a measurement performance test, which proved that a temperature gradient in deionized water could be reliably measured and also indicated that our optical setup was reliable and robust. We believe that the measurement precision, reliability, and robustness of our setup make it a good choice to be a prototype to measure the vapor density distribution of droplets in the TPSR of CSS. In particular, our optical setup represents a prototype layout, which could be further engineered in the future. When making the reference beam coincide with the objective beam's curvature, our setup, to the best of our knowledge, could obtain better contrast fringes in the holograms. This will be the subject of further investigation, together with further setup optimization to improve measurement reliability and precision. We also note that the droplet inner and outer gradients could be analyzed and inversed with an appropriate light scattering model under certain conditions [54]. Further research will explore this assumption in the future.

Acknowledgment. The authors express their gratitude to EditSprings [55] for the expert linguistic services provided.

Disclosures. The authors declare no conflicts of interest.

Data Availability. Data underlying the results presented in this paper are available in Ref. [46].

REFERENCES

1. C. Falsetti, M. Magnini, and J. R. Thome, "Hydrodynamic and thermal analysis of a micro-pin fin evaporator for on-chip two-phase cooling of high-density power micro-electronics," Appl. Therm. Eng. **130**, 1425–1439 (2018).
2. Z. Zhong, Z. Li, K. Chakrabarty, T. Ho, and C. Lee, "Micro-electrode-dot-array digital microfluidic biochips: technology, design automation, and test techniques," IEEE Trans. Biomed. Circuits Syst. **13**, 292–313 (2018).
3. T. J. Rector, J. W. Steele, and G. Bue, "Performance of a water recirculation loop maintenance device and process for the advanced spacesuit water membrane evaporator," in *International Conference on Environmental Systems AIAA 2013-3308* (2014), pp. 1–14.
4. R. G. Larson, "Transport and deposition patterns in drying sessile droplets," AIChE J. **60**, 1538–1571 (2014).
5. Z. Beiki, M. Taajobian, and A. Jahanian, "Efficient mapping of DNA logic circuits on parallelized digital microfluidic architecture," in *19th International Symposium on Computer Architecture and Digital Systems (CADS)* (2017), pp. 1–6.
6. V. Y. Levashov and A. P. Kryukov, "Numerical simulation of water droplet evaporation into vapor-gas medium," Colloid J. **79**, 647–653 (2017).
7. L. Luo, Z. Jia, H. Yang, Z. Zhang, and M. Chen, "Evaporation characteristics of droplets on a gradient microhole-patterned surface," J. Mater. Sci. **53**, 1447–1454 (2018).
8. N. D. Patil and R. Bhardwaj, "Recent developments on colloidal deposits obtained by evaporation of sessile droplets on a solid surface," J. Indian Inst. Sci. **99**, 143–156 (2019).
9. Y. Li and M. Yoda, "An experimental study of buoyancy-Marangoni convection in confined and volatile binary fluids," Int. J. Heat Mass Transfer **102**, 369–380 (2016).
10. M. P. L. Sentis, F. R. A. Onofri, and F. Lamadie, "Bubbles, drops, and solid particles recognition from real or virtual photonic jets reconstructed by digital in-line holography," Opt. Lett. **43**, 2945–2948 (2018).
11. A. Sankaran and A. L. Yarin, "Evaporation-driven thermocapillary Marangoni convection in liquid layers of different depths," Int. J. Heat Mass Transfer **122**, 504–514 (2018).
12. M. Andersson, S. B. Beale, and W. Lehnert, "Dynamic contact angle modeling of droplet reattachment at the gas channel wall in polymer electrolyte fuel cells," eTransportation **1**, 100003 (2019).
13. M. Ouattara, F. Lamadie, M. P. L. Sentis, and F. R. A. Onofri, "Droplet sizing and mixture fraction measurement in liquid flows with rainbow-angle diffractometry," Appl. Opt. **56**, 8109–8120 (2017).
14. S. Dehaeck and P. Colinet, "Measuring vapour cloud concentrations with digital holography," in *Biomedical Optics and 3-D Imaging* OSA Technical Digest (Optical Society of America, 2012), paper DTu2C.2.
15. F. D. Bloss, M. Gunter, S. Su, and H. E. Wolfe, "Gladstone-Dale constants: a new approach," Canad. Mineral. **21**, 93–99 (1983).
16. E. Mathews, K. Wang, M. Wang, and E. J. Jumper, "The wavenumber spectra of aero-optical phase distortions by weakly compressible turbulence," Opt. Express **27**, 5670–5684 (2019).
17. S. Dehaeck, A. Rednikov, and P. Colinet, "Vapor-based interferometric measurement of local evaporation rate and interfacial temperature of evaporating droplets," Langmuir **30**, 2002–2008 (2014).
18. W. Sun, J. Zhao, J. Di, Q. Wang, and L. Wang, "Real-time visualization of Karman vortex street in water flow field by using digital holography," Opt. Express **17**, 20342–20348 (2009).

19. F. Boudaoud and M. Lemerini, "Using a Mach–Zehnder interferometer to deduce nitrogen density mapping," Chin. Phys. B **24**, 75205 (2015).
20. J. M. Desse and F. Olchewsky, "Digital Mach-Zehnder holographic interferometer using pulsed laser for analyzing large flow fields," in *Imaging and Applied Optics 2016*, OSA Technical Digest (online) (Optical Society of America, 2016), paper DW1H.6.
21. F. Olchewsky, J. M. Desse, and P. Picart, "Off-axis digital holography spatial carrier frequency filtering," in *Imaging and Applied Optics 2016*, OSA Technical Digest (online) (Optical Society of America, 2016), paper DW1H.4.
22. J. C. Li, Z. J. Peng, and J. B. Chen, "Application of eliminating zero-order diffraction light in wavefront reconstruction of inverse diffraction computation," Optoelectron. Lett. **2**, 379–382 (2006).
23. Y. Zhang, J. Zhao, J. Di, H. Jiang, Q. Wang, J. Wang, Y. Guo, and D. Yin, "Real-time monitoring of the solution concentration variation during the crystallization process of protein-lysozyme by using digital holographic interferometry," Opt. Express **20**, 18415–18421 (2012).
24. V. Lédl, T. Vít, R. Doleček, and P. Psota, "Digital holographic interferometry used for identification of 2D temperature field," in Vol. **25** of *International Conference Experimental Fluid Mechanics 2010* (2012), pp. 1–6.
25. T. Kakue, R. Yonesaka, T. Tahara, Y. Awatsuji, K. Nishio, S. Ura, T. Kubota, and O. Matoba, "High-speed phase imaging by parallel phase-shifting digital holography," Opt. Lett. **36**, 4131–4133 (2011).
26. J. M. Dessel, F. Olchewsky, Z. Essaïdi, F. Nicolas, D. Donjat, F. Champagnat, F. Leopold, F. Jagusinski, D. Klatt, and P. Picart, "Investigation of high density gradients flows by pulsed digital holographic interferometry," in *Digital Holography and 3-D Imaging* (2017), paper M4A.1.
27. T. Fukuda, Y. Wang, P. Xia, Y. Awatsuji, T. Kakue, K. Nishio, and O. Matoba, "Three-dimensional imaging of distribution of refractive index by parallel phase-shifting digital holography using Abel inversion," Opt. Express **25**, 18066–18071 (2017).
28. F. Olchewsky, Z. Essaïdi, J. M. Desse, F. Nicolas, F. Champagnat, and P. Picart, "3D gas density reconstruction by digital holographic interferometry," in *Digital Holography and 3-D Imaging* (2017), paper Th2A.3.
29. F. Olchewsky, F. Champagnat, and J. Desse, "Multidirectional holographic interferometer for 3D gas density reconstruction," in *Imaging and Applied Optics* (2018), paper 3W5G.4.
30. K. M. Aly and E. Esmail, "Refractive index of salt water: effect of temperature," Opt. Mater. **2**, 195–199 (1993).
31. A. N. Bashkatov and E. A. Genina, "Water refractive index in dependence on temperature and wavelength: a simple approximation," Proc. SPIE **5068**, 25823–25832 (2003).
32. W. Liu, P. G. Chen, J. Ouazzani, and Q. Liu, "Thermocapillary flow transition in an evaporating liquid layer in a heated cylindrical cell," Int. J. Heat Mass Transfer **153**, 119587 (2020).
33. B. Maciejewska and M. Piasecka, "Time-dependent study of boiling heat transfer coefficient in a vertical minichannel," Int. J. Numer. Methods Heat Fluid Flow **30**, 2953–2969 (2019).
34. W. Liu, Z. Zhu, and Q. Liu, "Ground experiment study of evaporation phase change for space experiment device of TZ-1 cargo spaceship," Chin. J. Space Sci. **36**, 481–486 (2016).
35. X. Liao, W. Wu, X. Zhang, and Z. He, "Study on the flow condensation of mixed gases of FC72 and Nitrogen," Chin. J. Space Sci. **36**, 536–541 (2016).
36. J. Li, Z. Fan, and Z. Peng, "Application research on the zoom system of digital holography," Acta Photon. Sin. **37**, 1420–1424 (2008).
37. P. Ferraro, S. D. Nicola, A. Finizio, G. Coppola, S. Grilli, C. Magro, and G. Pierattini, "Compensation of the inherent wave front curvature in digital holographic coherent microscopy for quantitative phase-contrast imaging," Appl. Opt. **42**, 1938–1946 (2003).
38. M. F. Schatz and G. P. Neitzel, "Experiments on thermocapillary instabilities," Annu. Rev. Fluid Mech. **33**, 93–127 (2001).
39. U. Schnars and W. Jueptner, *Digital Holography*, 1st ed. (Springer, 2005), p. 21.
40. E. Cuche, P. Marquet, and C. Depeursinge, "Spatial filtering for zero-order and twin-image elimination in digital off-axis holography," Appl. Opt. **39**, 4070–4075 (2000).
41. E. N. Leith and J. Upatnieks, "Reconstructed wavefronts and communication theory," J. Opt. Soc. Am. **52**, 1123–1130 (1962).
42. J. Wang, J. Zhao, C. Qin, J. Di, A. Rauf, and H. Jiang, "Digital holographic interferometry based on wavelength and angular multiplexing for measuring the ternary diffusion," Opt. Lett. **37**, 1211–1213 (2012).
43. M. A. Herráez, D. R. Burton, M. J. Lalor, and M. A. Gdeisat, "Fast two-dimensional phase-unwrapping algorithm based on sorting by reliability following a noncontinuous path," Appl. Opt. **41**, 7437–7444 (2002).
44. D. Kerr, G. H. Kaufmann, and G. E. Galizzi, "Unwrapping of interferometric phase-fringe maps by the discrete cosine transform," Appl. Opt. **35**, 810–816 (1996).
45. Q. Wen, J. Shen, R. Gieleciak, K. H. Michaelian, J. H. Rohling, N. G. C. Astrath, and M. L. Baessoand, "Temperature coefficients of the refractive index for complex hydrocarbon mixtures," Int. J. Thermophys. **35**, 930–941 (2014).
46. D. R. Lide, ed., *CRC Handbook of Chemistry and Physics*, 82nd ed. (Taylor and Francis, 2001), pp. 10–218.
47. P. Schiebener and J. Straub, "Refractive index of water and steam as function of wavelength, temperature and density," J. Phys. Chem. Ref. Data **19**, 677–717 (1990).
48. E. J. Jumper and S. Gordeyev, "Physics and measurement of aero-optical effects: past and present," Annu. Rev. Fluid Mech. **49**, 419–441 (2017).
49. M. D. White, "High-order parabolic beam approximation for aero-optics," J. Comput. Phys. **229**, 5465–5485 (2010).
50. P. Giacomo, "Equation for the determination of the density of moist air (1981)," Metrologia **18**, 33–40 (1982).
51. R. S. Davis, "Equation for the determination of the density of moist air (1981/91)," Metrologia **29**, 67–70 (1992).
52. Organisation Internationale de Métrologie Légale, "Weights of classes E_1, E_2, F_1, F_2, M_1, M_{1-2}, M_2, M_{2-2}, M_{2-3}, and M_3. Part 1: Metrological and technical requirements," OIML.R 111-1 (2004), p. 76.
53. G. Mandal, A. Kumar, D. C. Sharma, and H. Kumar, "Comparative analysis of different air density equations," MAPAN **28**, 51–62 (2013).
54. F. Onofri, G. Gréhan, and G. Gouesbet, "Electromagnetic scattering from a multilayered sphere located in an arbitrary beam," Appl. Opt. **34**, 7113–7124 (1995).
55. EditSprings, https://www.editsprings.com/.